THE JOURNAL OF PHYSICAL CHEMISTRY C
A JOURNAL OF THE AMERICAN CHEMICAL SOCIETY

pubs.acs.org/JPCC

Article

High-Temperature Photoluminescence Enhancement up to 350 K of Monophase α-$FAPbI_3$ Quantum Dots Synthesized via Tailored Hot Injection

Nurwarrohman Andre Sasongko, Safira Arta Paramita, Jaeseong Heo, Eugene Park, Sebastian E. Reyes-Lillo, Joonkyung Jang, and Myeongkee Park*

Cite This: *J. Phys. Chem. C* 2025, 129, 15342−15350

Read Online

ACCESS | Metrics & More | Article Recommendations | Supporting Information

ABSTRACT: In this work, we developed a tailored hot-injection method to establish optimal synthesis conditions for purified monophase α-$FAPbI_3$ quantum dots (QDs). By precisely tuning the ligand ratio, washing solvent ratio, and growth temperature, we successfully synthesized highly uniform QDs (10.4 ± 1.1 nm) with dominant (001), (002), and (003) facets, high crystallinity, and improved photoluminescence (PL) lifetimes (~150 ns). By employing temperature-dependent PL on the phase-pure α-$FAPbI_3$ QDs, we investigated the phase-transition behavior. The α-$FAPbI_3$ QDs exhibit sequential phase transitions from γ-tetragonal-1 to β-tetragonal-2 to α-cubic at 140 and 250 K, respectively. Notably, the α-cubic phase exhibits a remarkable enhancement in PL intensity up to 350 K, indicating an improved charge-carrier mobility at elevated temperatures. These findings provide new insights into the structure−property relationships of monophase α-$FAPbI_3$ and support their potential for high-performance solar cell applications operating under thermal stress.

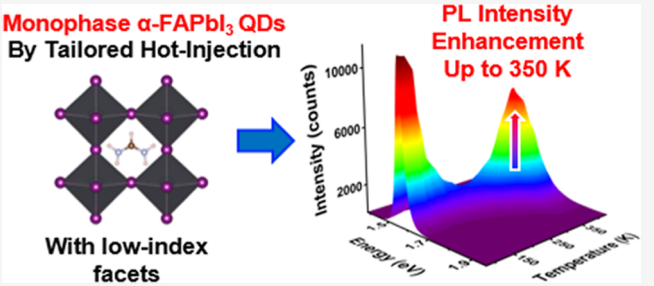

INTRODUCTION

A formamidinium-based organic−inorganic lead iodide perovskite ($CH(NH_2)_2PbI_3$, $FAPbI_3$) has emerged as a leading candidate in the perovskite solar cell category because of its higher ambient stability and longer charge-carrier lifetime compared to methylammonium-based perovskite ($MAPbI_3$) analogues.[1−6] This enhanced performance is partly attributed to the relatively larger grain size of $FAPbI_3$, on the order of micrometers, which contributes to higher stability and improved photoelectric properties compared to $MAPbI_3$ thin films.[7−13]

However, $FAPbI_3$ exhibits two distinct morphs at room temperature: photo-active α-phase and photo-inactive δ-phase.[4−6] The former is known as a black phase, which possesses desirable optoelectronic properties, while the latter is a yellow phase showing poor photoelectric performance to be avoided in applications.[14−16] Although postannealing can partially recover α-$FAPbI_3$ from δ-domains, a significant fraction becomes irreversibly stabilized, limiting practical applications.[4,17] In particular, the formation of the δ-phase can be easily observed in bulky thin films due to the intrinsic polycrystalline feature and grain boundaries containing serious structural vulnerability induced by exposure to ambient oxygen, humidity, and intense light, even during optical measurements.[18−22]

These issues hinder the direct investigation of the intrinsic optical behavior of pure α-$FAPbI_3$, as δ-phase contributions are difficult to eliminate and introduce charge-trapping heterogeneity. To address this issue, strategies such as mixing of halogens and organic cation additives have been employed to increase grain sizes (>2 μm) and suppress δ-phase formation.[23,24] However, these modifications do not fully prevent δ-phase formation, and remaining domains still serve as charge trap centers, significantly compromising optoelectronic performance.[24−26]

To gain physical−chemical insights into the intrinsic properties of pristine α-phase $FAPbI_3$, recent efforts have focused on nanoscale quantum dots (QDs) as an alternative to bulk thin films to overcome the phase instability issues inherent in bulk materials.[27−30] These QDs offer a nearly defect-free single-crystalline domain, effectively minimizing structural inhomogeneity. Moreover, their colloidal nature allows efficient passivation by surface ligands in nonpolar solvents, which provides protection from ambient degradation. With their tunable surface chemistry, QDs offer improved

Received: July 24, 2025
Revised: July 30, 2025
Accepted: July 31, 2025
Published: August 7, 2025

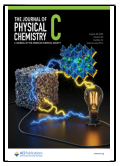

control over defect formation, thereby enhancing the stability of the α-phase.[29,30]

However, the synthesis of phase-pure α-$FAPbI_3$ QDs remains highly sensitive to reaction conditions.[30] Incomplete surface ligand passivation during synthesis can lead to surface instability, which correlates with reduced charge-carrier mobility due to faster exciton recombination at complex surface facets.[31−35] Both precise temperature control and careful purification procedures are also essential to achieve and maintain the phase stability of α-$FAPbI_3$ QDs.[30,31]

In this study, we address this gap by synthesizing highly uniform, monophase α-$FAPbI_3$ QDs via a tailored hot-injection method. By optimizing the oleylamine-to-oleic acid (OAm:OA) ligand ratio, acetonitrile-to-toluene washing solvent ratio, and growth temperature, we successfully suppress the δ-phase formation and obtain QDs with high crystallinity and dominant (001), (002), and (003) crystal facets. Temperature-dependent PL spectroscopy revealed a clear enhancement in PL intensity up to 350 K, uniquely in phase-pure α-$FAPbI_3$ by using temperature-dependent PL and Raman spectroscopies. These results provide crucial insights into the temperature-dependent structure−property relationships of $FAPbI_3$ QDs and highlight their potential for thermally robust, high-efficiency optoelectronic devices.

RESULTS AND DISCUSSION

We synthesized $FAPbI_3$ QDs with varying OAm:OA ratios of (1:2, 1:3, and 1:4 (v/v)), as the ratio is crucial in controlling the crystallinity and stability of the QDs.[36−38] Figure 1a shows the XRD patterns of the QDs, predominantly exhibiting (001), (002), and (003) crystal facets. Among the three ratio conditions, the QDs synthesized with a 1:3 OAm:OA ratio exhibit the highest crystallinity, as indicated by the narrowest full width at half-maximum (fwhm) values of the (001) and (002) peaks at approximately 0.37 and 0.44, respectively.

In contrast, the QDs synthesized with a 1:2 OAm:OA ratio showed a more amorphous structure, with broader fwhm values of 0.56 and 0.60 for the (001) and (002) planes, respectively. This is attributed to a relatively higher concentration of OAm, which facilitates the formation of protonated OAm^+ cations that can be substituted for FA^+ cations, disrupting the perovskite lattices.[39] In addition, a lower OA concentration reduces the formation of FA−oleate complexes that act as mobile and soluble A-site precursors.[40] This limitation decreases the FA^+ mobility during synthesis, resulting in uneven nucleation and reduced crystallinity. However, an excessive amount of OA, as in the 1:4 ratio, also negatively impacts crystallinity. The dense OA ligand shell sterically hinders crystal growth and prevents proper fusion of precursor species into an ordered lattice. Additionally, excess OA complicates purification, as the resulting OA-rich ligand shell promotes QD dissolution in the antisolvent (Figure S1). Therefore, the 1:3 OAm:OA ratio offers an optimal balance for achieving high crystallinity in the $FAPbI_3$ QDs.

Figure 1b shows that increasing OA concentration induces a redshift in the PL peak, indicating larger QDs due to quantum confinement effect. This size increase of QDs by higher OA concentration is attributed to the two-step dissolution−recrystallization mechanism reported in previous studies.[41,42] Time-resolved PL (TRPL) in Figure 1c further confirms that the optimal ratio of the OAm:OA is 1:3, as this sample exhibits the longest PL lifetime (~150 ns), significantly longer than those synthesized with the 1:2 (~95 ns) and 1:4 (~70 ns)

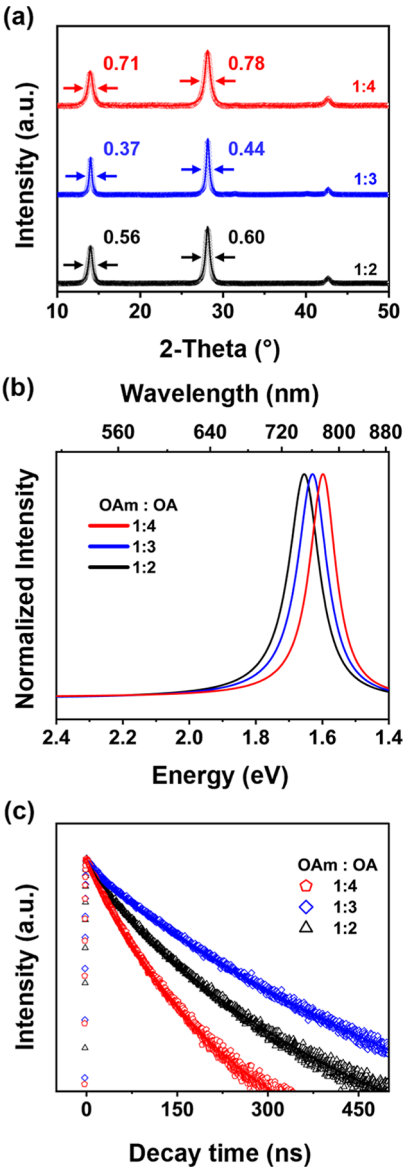

Figure 1. (a) XRD patterns, (b) steady-state PL spectra, and (c) time-resolved PL of $FAPbI_3$ QDs synthesized at a growth temperature of 100 °C with varying oleylamine-to-oleic acid (OAm:OA) volume ratios (1:2, 1:3, and 1:4) and purified using an acetonitrile:toluene volume ratio of 1:20. The 1:3 condition exhibits the narrowest diffraction, the highest PL intensity, and the longest carrier lifetime, indicating optimal crystallinity and surface passivation.

ratios. The longest PL lifetime of the 1:3 sample shows reduced nonradiative recombination and improved surface passivation, which correlates with its higher crystallinity observed in the XRD results (Figure 1a). In contrast, the shorter lifetimes of the 1:2 and 1:4 samples result from increased nonradiative recombination correlated to poorer crystallinity (in the case of 1:2) or surface ligand oversaturation (in the case of 1:4), both of which hinder efficient radiative recombination. These results confirm that a balanced OAm:OA ratio of 1:3 is optimal for achieving highly crystalline and optoelectronically superior $FAPbI_3$ QDs.

We investigated the influence of ligand removal during washing on nonradiative recombination sites using XRD and TRPL. In the washing step, we used toluene as a nonpolar solvent to effectively remove excess ligands and acetonitrile as

https://doi.org/10.1021/acs.jpcc.5c05144
J. Phys. Chem. C 2025, 129, 15342−15350

a polar solvent to promote QD precipitation.[30,32] Recent studies have reported different acetonitrile:toluene ratios (1:1 and 1:4) during the washing process.[30,32] To explore the limits of ligand removal without degrading crystallinity and reducing the PL lifetime, we extended the acetonitrile:toluene ratio range to 1:1, 1:10, and 1:20.

Figure 2a shows the XRD patterns of $FAPbI_3$ QDs washed using different acetonitrile:toluene ratios (1:1, 1:10, and 1:20

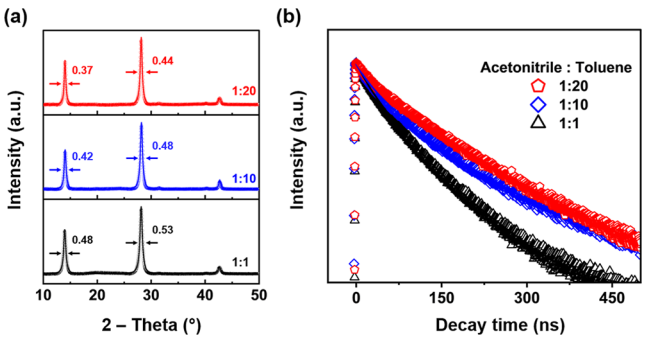

Figure 2. (a) XRD patterns and (b) time-resolved PL of $FAPbI_3$ QDs synthesized at a growth temperature of 100 °C with an OAm:OA volume ratio of 1:3 and purified using different acetonitrile:toluene volume ratios (1:1, 1:10, and 1:20). The 1:20 condition exhibits the narrowest diffraction peaks and the longest carrier lifetime, indicating optimal crystallinity and surface passivation.

v/v). The QDs washed with the 1:20 ratio exhibit the narrowest fwhm values: 0.37 for the (001) and 0.44 for the (002) planes. In comparison, the 1:10 ratio results in broader peaks with fwhm values of 0.42 (001) and 0.48 (002), while the 1:1 ratio gives the broadest peaks, with fwhm values of 0.48 (001) and 0.53 (002). These results demonstrate that increasing the toluene content enhances the crystallinity, as evidenced by sharper and narrower diffraction peaks. Higher toluene concentration leads to more effective removal of surface ligands, thereby promoting improved crystal growth.[30] In contrast, excessive acetonitrile causes particle aggregation during precipitation, resulting in structural disorder.[30] Thus, the 20× toluene content is optimal for obtaining highly crystalline $FAPbI_3$ QDs during the washing step.

Figure 2b shows PL lifetime decay curves further supporting the selection of the acetonitrile:toluene of 1:20 washing ratio. The QDs purified with 1:1 exhibit a short average PL lifetime of 80 ns, arising from surface defects and poor crystallinity. Increasing the toluene content to the 1:10 ratio significantly extends the PL lifetime to 135 ns, while the 1:20 ratio yields the longest lifetime of 150 ns. Thus, a higher toluene content improves the crystal quality and causes fewer surface trap states, reducing nonradiative recombination. However, adding toluene in a more than 1:20 ratio could lead to the partial dissolution of QDs, reducing the overall yield and potentially compromising size and shape uniformity. In this study, the acetonitrile:toluene ratio of 1:20 is suggested as the optimal purification condition for producing $FAPbI_3$ QDs with improved crystallinity and prolonged PL lifetimes. This emphasizes the critical role of solvent composition during purification in determining both the structural and the optoelectronic quality of $FAPbI_3$ QDs.

We then investigated the effect of growth temperature (25, 50, and 100 °C) on the structural uniformity and phase stability of $FAPbI_3$ QDs using the optimal synthesis conditions (OAm:OA of 1:3 and acetonitrile:toluene of 1:20 washing solution). As shown in Figure 3a, QDs synthesized at 25 °C exhibit mixed phases, including the α-phase $FAPbI_3$ perovskite along with peaks corresponding to the nonperovskite δ-$FAPbI_3$ and PbI_2, indicating incomplete conversion to the α-$FAPbI_3$. At lower temperatures, the higher concentration of the OAm^+ ligand tends to replace the FA^+ cation, destabilizing the α-$FAPbI_3$ phase.[41] Raising the growth temperature of 50 °C results in the emergence of distinct α-$FAPbI_3$ peaks corresponding to (001), (002), (012), (022), and (003) facets. Further increasing the growth temperature to 100 °C leads to an XRD pattern that clearly shows the (001), (002), and (003) planes. This suggests preferred growth orientation along these low-index facets, which are thermodynamically more stable and less susceptible to defect formation. While typical hot-injection synthesis is performed around 80 °C, XRD patterns in other studies still show notable (012) and (022) peaks,[31,32] implying that 100 °C offers improved facet control and enhanced crystal quality.

Our overall synthesis optimization significantly affects the optical properties, as shown by PL decays in Figure 3b. The QDs synthesized at 25 °C exhibited the shortest average PL lifetime (~60 ns), due to the presences of PbI_2 and δ-$FAPbI_3$ phases, which contribute to nonradiative recombination. The QDs synthesized at 50 °C exhibit an average PL lifetime of approximately 70 ns, which is consistent with recent reports that highlight the exposure of (012) and (022) facets.[30,31] In contrast, the QDs synthesized at 100 °C show a significantly longer PL lifetime of ~150 ns, more than twice that of the 50 °C sample and exceeding the typical range of 20−100 ns reported for $FAPbI_3$ QDs.[30−32] This substantial enhancement is attributed to the dominant exposure of the (001), (002), and (003) facets at higher synthesis temperatures, which are known to have fewer surface defects and improved passivation characteristics.[33−35] These well-defined facets effectively suppress trap-assisted recombination, resulting in extended carrier lifetimes and enhanced photoluminescence performance.[33−35]

Figure 3c shows a redshift of the PL peaks with increasing temperature, attributed to the larger QD sizes observed in Figure 3d−i. The average dimensions of the QDs synthesized at 25, 50, and 100 °C are approximately 7.6 ± 2.4, 9.5 ± 1.6, and 10.4 ± 1.1 nm, respectively. Specifically, the QDs synthesized at 25 °C exhibit the broadest PL peak, consistent with the largest size distribution (fwhm = 5.7 nm) observed in the TEM image (Figure 3g). In contrast, higher synthesis temperatures improved size uniformity, showing fwhm's of 3.7 and 2.7 nm for QDs synthesized at 50 and 100 °C, respectively. Furthermore, the inset of Figure 3f confirms the enhanced crystallinity at 100 °C, as evidenced by the (002) lattice distance of 6.38 Å. High-temperature synthesis at around 100 °C facilitates uniform QD formation with improved crystallinity in the hot-injection process, due to reduced nucleation density and increased atomic mobility.[43,44]

We employed temperature-dependent PL spectroscopy to investigate phase transitions in a pristine α-$FAPbI_3$ QD, because changes in crystal symmetry during a phase transition result in alteration in the bandgap energy, spectral broadening, and PL intensity.[21,45,46] Specifically, the temperature-dependent slope of the bandgap shift identifies phase transition associated with electron−phonon interactions and lattice dynamics.[46] Similarly, changes in the fwhm slope reflect the degree of conformational lattice disorder and carrier scattering

https://doi.org/10.1021/acs.jpcc.5c05144
J. Phys. Chem. C 2025, 129, 15342−15350

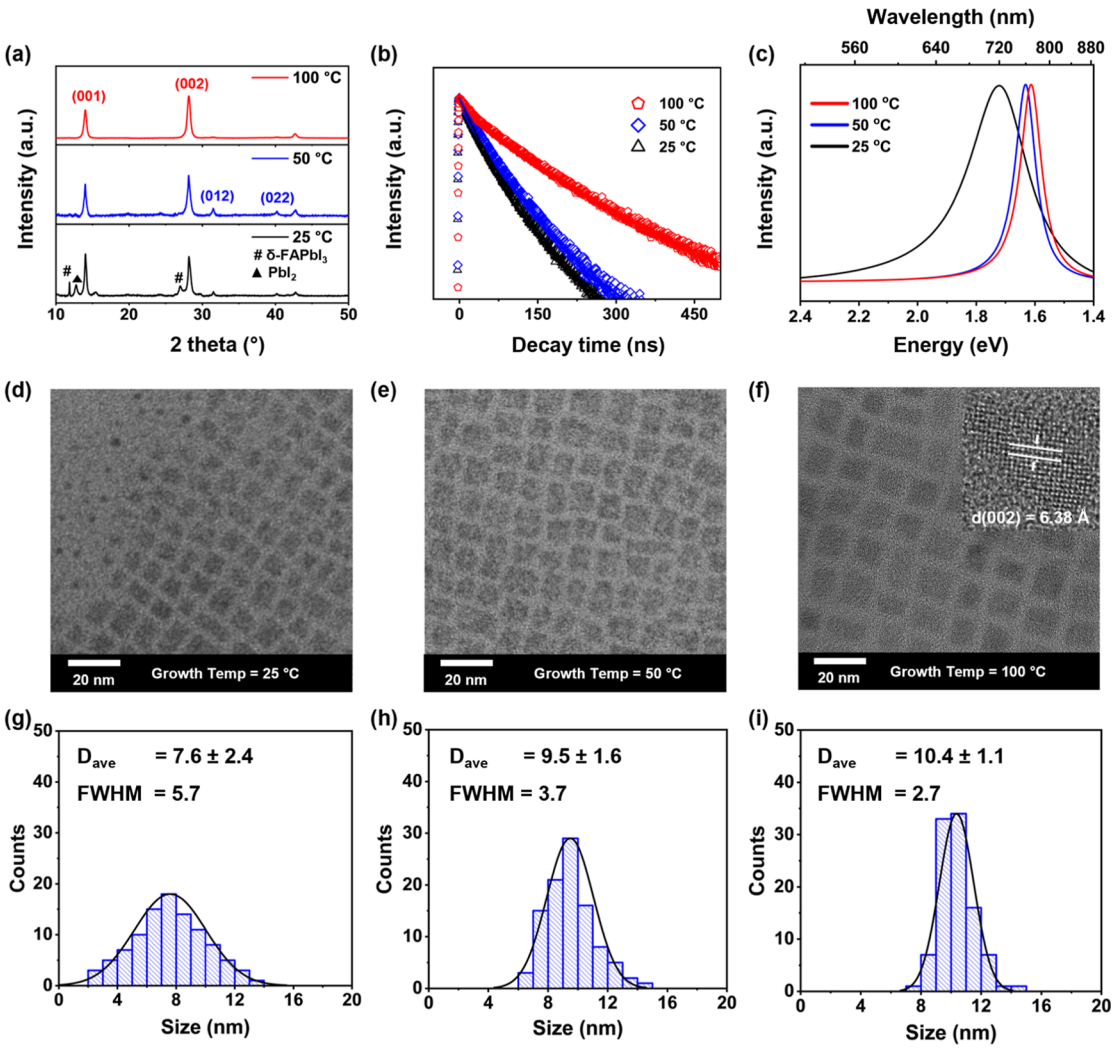

Figure 3. (a) XRD patterns, (b) time-resolved PL, (c) steady-state PL spectra, (d–f) TEM images, and (g–i) size distributions of $FAPbI_3$ QDs synthesized at different growth temperatures (25, 50, and 100 °C). The symbols ▲ and # indicate the peaks corresponding to PbI_2 and δ-$FAPbI_3$, respectively. All QDs were with an OAm:OA volume ratio of 1:3 and purified using an acetonitrile:toluene volume ratio of 1:20. The QDs synthesized at 100 °C exhibited optimal crystallinity and uniformity. The inset in panel (f) shows a lattice spacing of 6.38 Å, corresponding to the (002) plane of $FAPbI_3$.

in each phase.[47] In addition, changes in PL intensity are also linked to symmetry-dependent exciton recombination.[32,48] These temperature-dependent PL parameters are complementary to the phase transitions.

We studied the phase evolution of $FAPbI_3$ QDs using temperature-dependent PL from 80 to 430 K. Figure 4a,b shows the phase transitions from tetragonal-1 (γ) to tetragonal-2 (β) at 140 K and tetragonal-2 (β) to cubic (α) at 250 K. The γ–β transition is indicated by a redshift of the PL peak below 140 K, followed by a blueshift above this temperature. This transition is also supported by a sharp decrease in PL intensity and a gradual broadening of fwhm. The β–α phase transition is characterized by an increase in PL intensity above 250 K, accompanied by a continuous blueshift and gradual fwhm broadening.

We fitted the PL spectra with Lorentzian functions and extracted the temperature-dependent bandgap energy, PL intensity, and fwhm. Figure 5a shows a redshift in the PL peak of γ–$FAPbI_3$, with a slope of -7.9×10^{-5} eV/K, observed between 80 and 140 K. This redshift is attributed to an enhanced electron–phonon coupling, which effectively reduces the bandgap and promotes lower energy emission.[45,49] As the temperature exceeds 140 K, the PL peak exhibits a blueshift with a slope of 4.32×10^{-4} eV/K, indicating the transition to the β phase. This blueshift is primarily driven by thermal expansion of the crystal lattice, resulting in a bandgap energy increase.[48,50] This transition is further supported by changes in the fwhm shown in Figure 5b. The fwhm slope decreases from 4.01×10^{-4} eV/K in the γ phase to 2.29×10^{-4} eV/K in the β phase.

Figure 5c shows two distinguished decreasing patterns in PL intensity. In the γ phase, the PL decrease is attributed to more activated nonradiative recombination that arises from strong electron–phonon interactions by heat, resulting in fewer electrons transitioning to the radiative state.[51,52] Upon transition to the β phase, the PL intensity continues to decline, albeit at a reduced rate. It is also due to the effects of the thermal expansion and the associated bandgap widening, reducing the efficiency of radiative recombination.[48,50] Additionally, thermally activated dynamic displacements of inorganic framework in the β phase may lead to additional nonradiative losses, resulting in the decrease in PL intensity.[15]

https://doi.org/10.1021/acs.jpcc.5c05144
J. Phys. Chem. C 2025, 129, 15342–15350

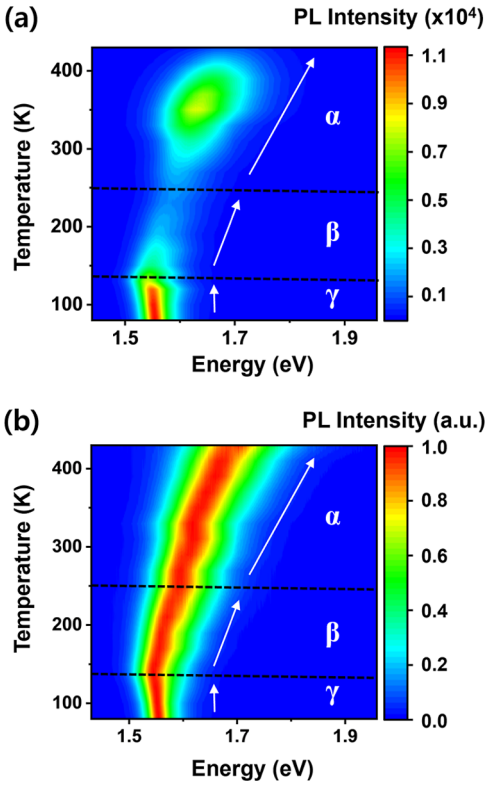

Figure 4. Temperature-dependent PL contour plots of $FAPbI_3$ QDs measured from 80 to 430 K. (a) Absolute and (b) normalized integrated PL spectra.

This transition is further confirmed by the temperature-dependent Raman data shown in Figure S2. Temperature-dependent Raman shows that the peak at 120 cm^{-1}, assigned as the I−Pb−I stretching, blue-shifted as the temperature increases from 80 to 140 K and red-shifted at temperatures above 140 K, indicating the transition from γ to β. The transition temperature γ-to-β at 140 K is consistent with previous studies of $FAPbI_3$, as summarized in Table S1.[53−57]

The phase transition temperature of $FAPbI_3$ QDs from β to α occurs at 250 K, as indicated by the change in the PL shift slope, fwhm slope, and PL intensity enhancement. The PL shift slope decreases slightly from 4.32×10^{-4} eV/K to 3.97×10^{-4} eV/K. In parallel, the fwhm slope reduces from 2.29×10^{-4} eV/K to 1.69×10^{-4} eV/K, implying a narrower spectral width due to improved crystalline order in the cubic α-phase. Notably, the phase transition temperature of $\beta \rightarrow \alpha$ in $FAPbI_3$ QDs is lower than that of bulk $FAPbI_3$, which undergoes this transition at around 285 K (Table S1).[53−57] It is suggested that the higher structural uniformity and lower defect density in QDs reduce the energy barrier for the phase transition. In contrast, bulk pristine $FAPbI_3$ without additives often contains an inhomogeneous mixture of phases, including structural defects and even δ-phase impurities.[24,58,59]

The $\beta \rightarrow \alpha$ transition is further supported by the PL intensity enhancement in α-phases shown in Figure 5c, which aligns with previous studies reporting an increase in PL intensity and lifetime during this transition.[60−63] This increase in PL intensity is attributed to lower defect density and more efficient carrier recombination in the α-cubic phase than in the β-tetragonal phase.[64] Interestingly, the PL intensity continuously increases up to 350 K, while recent studies for $FAPbI_3$ nanocrystals show the PL intensity enhancement only up to

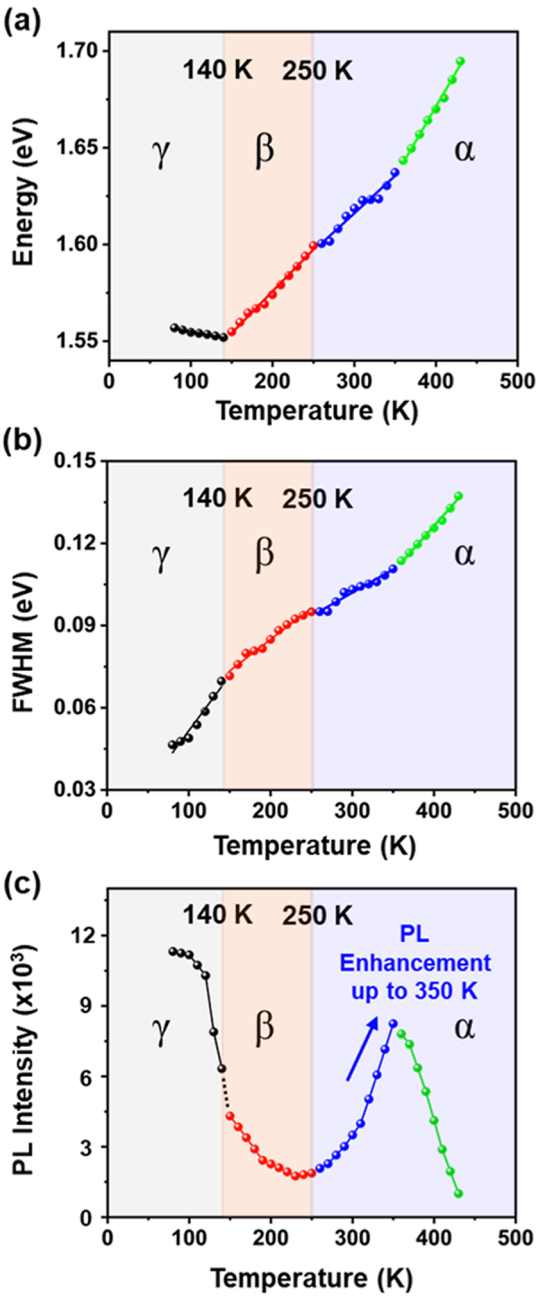

Figure 5. (a) Temperature-dependent PL peak shift, (b) full-width at half-maximum (fwhm), and (c) integrated PL intensity of α-$FAPbI_3$ QDs measured from 80 to 430 K. Distinct phase transitions from γ to β to α phases are observed at 140 and 250 K. Within the α-phase, the PL intensity increases steadily up to 350 K.

250 K.[31,60] This discrepancy is primarily attributed to differences in the facet orientation. In our study, the QDs predominantly expose the low-index (001) and (002) facets, while prior reports showed dominant (012) and (022) facets, with PL intensity reaching a maximum at 250 K, followed by a gradual decline up to 310 K and a sharp drop thereafter.[31] In addition, we have also measured that the PL intensity is highly stable at 350 K (Figure S3). These results demonstrate that phase-pure α-$FAPbI_3$ quantum dots with well-defined low-index facets exhibit a thermally enhanced PL response sustained up to 100 K higher than previously reported.[31]

https://doi.org/10.1021/acs.jpcc.5c05144
J. Phys. Chem. C 2025, 129, 15342−15350

$FAPbI_3$ perovskites exhibit facet-dependent surface stability and defect characteristics. The (001) facet, as a low-index plane, provides balanced ionic termination and fewer unsaturated bonds, resulting in lower defect densities.[33,35] In contrast, high-index facets like (110) and (111) often contain unsaturated Pb−I bonds and structural irregularities that generate surface traps.[65,66] Thus, the predominant exposure of the (001), (002), and (003) facets in our QDs is expected to reduce surface defects and suppress nonradiative recombination, enhancing the PL efficiency and carrier lifetime.

This continued PL enhancement may also be partially attributed to thermal lattice expansion, which can reduce surface trap density by relieving defect-induced lattice strain, thereby suppressing nonradiative pathways.[67] Furthermore, elevated temperatures may facilitate exciton delocalization and thermal activation of bright emissive states, synergistically boosting the PL intensity in the α-cubic phase.[68] Such a behavior is particularly favorable in QDs with low-index facets that further minimize trap-assisted recombination. Thus, our synthesis optimization leads to improved optoelectronic properties by promoting the formation of optically favorable facets. It is particularly beneficial for PL increase within the temperature range of 250 to 350 K, practical operational conditions for device applications.[69−,74]

Figure 5c shows a notable decrease in PL intensity at temperatures above 350 K due to excessive thermal expansion.[15,31] This is evidenced by the steeper slope of the bandgap energies (PL blueshift), which increases from 3.97×10^{-4} eV/K to 7.26×10^{-4} eV/K (Figure 5a), indicating a stronger thermal expansion effect of the Pb−I framework. Such expansion can promote hot−phonon interaction with excitons, increasing the nonradiative recombination rate.[31] In addition, the fwhm slope increases from 1.69×10^{-4} eV/K to 3.35×10^{-4} eV/K, indicating enhanced exciton−phonon coupling and larger energetic disorder (Figure 5b).[31]

Scheme 1 shows a summary of the complete phase transitions of $FAPbI_3$ QDs as determined in our study referring to the crystal parameters reported recently.[15] At temperatures below 140 K, $FAPbI_3$ exists in the tetragonal γ-phase ($P4/mbm$, $a = b = 8.88$ Å and $c = 6.28$ Å).[15] The transition from the γ-phase to tetragonal β-phase ($P4/mbm$, $a = b = 8.92$ and $c = 6.33$ Å) occurs at 140 K.[15] In addition, the β-phase transforms into the α-cubic phase ($Pm3m$, $a = b = c = 6.36$ Å) at 250 K. The regime between 250 and 350 K can be described as the thermally activated PL enhancement regime of α-phase $FAPbI_3$, characterized by the continuous PL intensity growth. Then, excessive thermal effects accelerate the charge-carrier recombination at temperatures higher than 350 K, reducing the PL intensity.

CONCLUSION

In summary, we synthesized phase-pure, monodisperse α-$FAPbI_3$ QDs (~10.4 nm) via a tailored hot-injection method with precise ligand and growth condition control. These QDs exhibit excellent crystallinity, long PL lifetimes (~150 ns), and dominant low-index facets. Temperature-dependent PL and Raman spectroscopy revealed sequential phase transitions ($\gamma \rightarrow \beta \rightarrow \alpha$) at 140 and 250 K, respectively. Notably, an enhancement in the PL intensity was observed up to 350 K in the α-cubic phase. This is the first report of thermally enhanced PL intensity at elevated temperature in phase-pure α-$FAPbI_3$ QDs, offering valuable insights into their structural stability and potential for high-performance optoelectronic applications.

Scheme 1. Schematic Representation of the Temperature-Dependent Phase Evolution of $FAPbI_3$ QDs. Upon Sequential Transitions from the γ-Tetragonal Phase to the β-Tetragonal Phase (>140 K) and Subsequently to the α-Cubic Phase (>250 K), PL Intensity Increases up to 350 K. Beyond 350 K, However, Excessive Thermal Expansion Promotes Nonradiative Recombination, Resulting in a PL Intensity Decrease

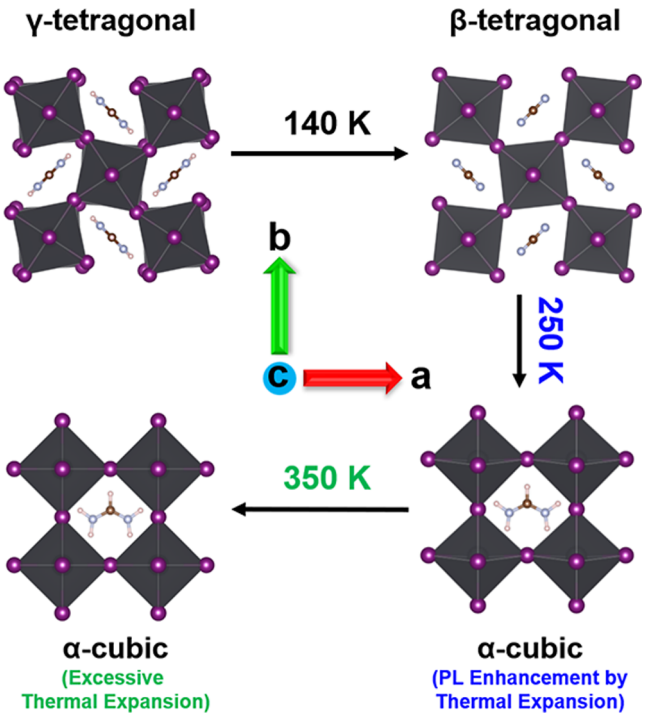

ASSOCIATED CONTENT

Supporting Information

The Supporting Information is available free of charge at https://pubs.acs.org/doi/10.1021/acs.jpcc.5c05144.

Experimental method, temperature-dependent Raman, summary of phase transition of $FAPbI_3$ in a recent study, and thermal PL stability of $FAPbI_3$ QDs at 350 K (PDF)

AUTHOR INFORMATION

Corresponding Author

Myeongkee Park − *BB21 Plus Program, Department of Chemistry, Pukyong National University, Busan 48513, Republic of Korea;* orcid.org/0000-0002-5307-2564; Email: bikeplay@pknu.ac.kr

Authors

Nurwarrohman Andre Sasongko − *BB21 Plus Program, Department of Chemistry, Pukyong National University, Busan 48513, Republic of Korea;* orcid.org/0000-0003-2228-3999

Safira Arta Paramita − *BB21 Plus Program, Department of Chemistry, Pukyong National University, Busan 48513, Republic of Korea*

Jaeseong Heo − *BB21 Plus Program, Department of Chemistry, Pukyong National University, Busan 48513, Republic of Korea*

Eugene Park − *BB21 Plus Program, Department of Chemistry, Pukyong National University, Busan 48513, Republic of Korea*

Sebastian E. Reyes-Lillo − *Departamento de Física y Astronomía, Universidad Andres Bello, Santiago 837-0136, Chile*

Joonkyung Jang − *Department of Nanoenergy Engineering, Pusan National University, Busan 46241, Republic of Korea;* orcid.org/0000-0001-9028-0605

Complete contact information is available at: https://pubs.acs.org/10.1021/acs.jpcc.5c05144

Notes

The authors declare no competing financial interest.

■ ACKNOWLEDGMENTS

This work was supported by the National Research Foundation of Korea (NRF) grant funded by Korea government (MSIT) (RS-2023-00220748) and the Global Joint Research Program funded by the Pukyong National University (202411650001). S.E.R.L. acknowledges ANID Fondecyt Regular grant number 1220986.

■ ABBREVIATIONS

FWHM	full-width at half-maximum
PL	photoluminescence
QDs	quantum dots
TRPL	time-resolved photoluminescence

■ REFERENCES

(1) Wang, D.; Chen, M.; Zhang, X.; Chao, L.; Niu, T.; Lv, Y.; Xing, G.; Xia, Y.; Li, M.; Zhang, H.; et al. Stabilization of Component-Pure α-$FAPbI_3$ via Volatile Additives for Stable Photovoltaics. *ACS Appl. Mater. Interfaces* **2023**, *15* (13), 16818−16827.

(2) Park, J.; Kang, B. J.; Seo, G.; Kim, J.; Park, T. G.; Nam, S.; Yoo, J. J.; Lee, K.; Jeong, Y. U.; Park, M.; et al. Cross-Correlation Between Crystallinity and Optoelectronic Properties of Mixed-Perovskite Thin Films Through Multiple Time-Resolved Spectroscopy. *Adv. Energy Mater.* **2024**, *15* (2), 2400225.

(3) Park, M.; Neukirch, A. J.; Reyes-Lillo, S. E.; Lai, M.; Ellis, S. R.; Dietze, D.; Neaton, J. B.; Yang, P.; Tretiak, S.; Mathies, R. A. Excited-State Vibrational Dynamics toward the Polaron in Methylammonium Lead Iodide Perovskite. *Nat. Commun.* **2018**, *9* (1), 2525.

(4) Ibaceta-Jaña, J.; Muydinov, R.; Rosado, P.; Vinoth Kumar, S. H. B.; Gunder, R.; Hoffmann, A.; Szyszka, B.; Wagner, M. R. Hidden Polymorphism of $FAPbI_3$ Discovered by Raman Spectroscopy. *Phys. Chem. Chem. Phys.* **2021**, *23* (15), 9476−9482.

(5) Binek, A.; Hanusch, F. C.; Docampo, P.; Bein, T. Stabilization of the Trigonal High-Temperature Phase of Formamidinium Lead Iodide. *J. Phys. Chem. Lett.* **2015**, *6* (7), 1249−1253.

(6) Bouich, A.; Torres, J. C.; Khattak, Y. H.; Baig, F.; Marí-Guaita, J.; Soucase, B. M.; Mendez-Blas, A.; Palacios, P. Bright Future by Controlling α/δ Phase Junction of Formamidinium Lead Iodide Doped by Imidazolium for Solar Cells: Insight from Experimental, DFT Calculations and SCAPS Simulation. *Surf. Interfaces.* **2023**, *40*, 103159.

(7) Yuan, J.; Hazarika, A.; Zhao, Q.; Ling, X.; Moot, T.; Ma, W.; Luther, J. M. Metal Halide Perovskites in Quantum Dot Solar Cells: Progress and Prospects. *Joule* **2020**, *4*, 1160−1185.

(8) Li, F.; Zhang, X.; Shi, J.; Jin, L.; Qiao, J.; Guo, J.; Yin, H.; Li, Y.; Yuan, J.; Ma, W. Solution-Mediated Hybrid $FAPbI_3$ Perovskite Quantum Dots for Over 15% Efficient Solar Cell. *Adv. Funct. Mater.* **2023**, *33* (40), 2302542.

(9) Zhang, X.; Huang, H.; Jin, L.; Wen, C.; Zhao, Q.; Zhao, C.; Guo, J.; Cheng, C.; Wang, H.; Zhang, L.; et al. Ligand-Assisted Coupling Manipulation for Efficient and Stable $FAPbI_3$ Colloidal Quantum Dot Solar Cells. *Angew. Chem., Int. Ed.* **2023**, *62* (5), No. e202214241.

(10) Azar, M. H.; Mohammadi, M.; Rezaei, N. T.; Aynehband, S.; Simchi, A. Effect of Silica Encapsulation on the Stability and Photoluminescence Emission of $FAPbI_3$ Nanocrystals for White-Light-Emitting Perovskite Diodes. *J. Alloys Compd.* **2022**, *907*, 164465.

(11) Tseng, Z. L.; Chen, L. C.; Chao, L. W.; Tsai, M. J.; Luo, D.; Al Amin, N. R.; Liu, S. W.; Wong, K. T. Aggregation Control, Surface Passivation, and Optimization of Device Structure toward Near-Infrared Perovskite Quantum-Dot Light-Emitting Diodes with an EQE up to 15.4%. *Adv. Mater.* **2022**, *34* (18), 2109785.

(12) Shen, J. H.; Yu, X. Q.; Tu, W. C. Multifunctional and High-Performance $FAPbI_3$ Quantum Dots/Graphene UV Photodetectors by the Modulation of Photoconductivity. *Adv. Opt. Mater.* **2023**, *11* (17), 2300410.

(13) Hasanzadeh Azar, M.; Mohammadi, M.; Rezaei, N. T.; Aynehband, S.; Shooshtari, L.; Mohammadpour, R.; Simchi, A. Stable Photodetectors Based on Formamidinium Lead Iodide Quantum Well Perovskite Nanoparticles Fabricated with Excess Organic Cations. *ACS Appl. Nano Mater.* **2021**, *4* (8), 7788−7799.

(14) Chen, T.; Foley, B. J.; Park, C.; Brown, C. M.; Harriger, L. W.; Lee, J.; Ruff, J.; Yoon, M.; Choi, J. J.; Lee, S.-H. Entropy-Driven Structural Transition and Kinetic Trapping in Formamidinium Lead Iodide Perovskite. *Sci. Adv.* **2016**, *2* (10), No. e1601650.

(15) Fabini, D. H.; Stoumpos, C. C.; Laurita, G.; Kaltzoglou, A.; Kontos, A. G.; Falaras, P.; Kanatzidis, M. G.; Seshadri, R. Reentrant Structural and Optical Properties and Large Positive Thermal Expansion in Perovskite Formamidinium Lead Iodide. *Angew. Chem., Int. Ed.* **2016**, *128* (49), 15618−15622.

(16) Shen, X.; Gallant, B. M.; Holzhey, P.; Smith, J. A.; Elmestekawy, K. A.; Yuan, Z.; Rathnayake, P. V. G. M.; Bernardi, S.; Dasgupta, A.; Kasparavicius, E.; et al. Chloride-Based Additive Engineering for Efficient and Stable Wide-Bandgap Perovskite Solar Cells. *Adv. Mater.* **2023**, *35* (30), 2211742.

(17) Sturdza, B. K.; Gallant, B. M.; Holzhey, P.; Duijnstee, E. A.; Von der Leyen, M. W.; Sansom, H. C.; Snaith, H. J.; Riede, M. K.; Nicholas, R. J. Direct Observation of Phase Transitions Between Delta- and Alpha-Phase $FAPbI_3$ via Defocused Raman Spectroscopy. *J. Mater. Chem. A* **2024**, *12*, 5406−5413.

(18) Duijnstee, E. A.; Gallant, B. M.; Holzhey, P.; Kubicki, D. J.; Collavini, S.; Sturdza, B. K.; Sansom, H. C.; Smith, J.; Gutmann, M. J.; Saha, S.; et al. Understanding the Degradation of Methylenediammonium and Its Role in Phase-Stabilizing Formamidinium Lead Triiodide. *J. Am. Chem. Soc.* **2023**, *145* (18), 10275−10284.

(19) Chen, H.; Chen, Y.; Zhang, T.; Liu, X.; Wang, X.; Zhao, Y. Advances to High-Performance Black-Phase $FAPbI_3$ Perovskite for Efficient and Stable Photovoltaics. *Small Struct.* **2021**, *2* (5), 2000130.

(20) Jiang, S.; Luan, Y.; Jang, J. I.; Baikie, T.; Huang, X.; Li, R.; Saouma, F. O.; Wang, Z.; White, T. J.; Fang, J. Phase Transitions of Formamidinium Lead Iodide Perovskite under Pressure. *J. Am. Chem. Soc.* **2018**, *140* (42), 13952−13957.

(21) Spanopoulos, I.; Ke, W.; Stoumpos, C. C.; Schueller, E. C.; Kontsevoi, O. Y.; Seshadri, R.; Kanatzidis, M. G. Unraveling the Chemical Nature of the 3D "Hollow" Hybrid Halide Perovskites. *J. Am. Chem. Soc.* **2018**, *140* (17), 5728−5742.

(22) Park, M.; Kornienko, N.; Reyes-Lillo, S. E.; Lai, M.; Neaton, J. B.; Yang, P.; Mathies, R. A. Critical Role of Methylammonium Librational Motion in Methylammonium Lead Iodide ($CH_3NH_3PbI_3$) Perovskite Photochemistry. *Nano Lett.* **2017**, *17* (7), 4151−4157.

(23) Shin, S.; Seo, S.; Jeong, S.; Sharbirin, A. S.; Kim, J.; Ahn, H.; Park, N. G.; Shin, H. Kinetic-Controlled Crystallization of α-$FAPbI_3$ Inducing Preferred Crystallographic Orientation Enhances Photovoltaic Performance. *Adv. Sci.* **2023**, *10* (14), 2300798.

(24) Kim, M.; Kim, G. H.; Lee, T. K.; Choi, I. W.; Choi, H. W.; Jo, Y.; Yoon, Y. J.; Kim, J. W.; Lee, J.; Huh, D.; et al. Methylammonium Chloride Induces Intermediate Phase Stabilization for Efficient Perovskite Solar Cells. *Joule* **2019**, *3* (9), 2179−2192.

(25) Kang, D. H.; Lee, S. U.; Park, N. G. Effect of Residual Chloride in $FAPbI_3$ Film on Photovoltaic Performance and Stability of Perovskite Solar Cell. *ACS Energy Lett.* **2023**, *8* (5), 2122−2129.
(26) Pham, H. T.; Yin, Y.; Andersson, G.; Weber, K. J.; Duong, T.; Wong-Leung, J. Unraveling the Influence of CsCl/MACl on the Formation of Nanotwins, Stacking Faults and Cubic Supercell Structure in FA-Based Perovskite Solar Cells. *Nano Energy* **2021**, *87*, 106226.
(27) Ryu, H. J.; Shin, M.; Park, M.; Lee, J. S. In Situ Tetraalkylammonium Ligand Engineering of Organic-Inorganic Hybrid Perovskite Nanoparticles for Enhancing Long-Term Stability and Optical Tunability. *Langmuir* **2022**, *38* (44), 13448−13455.
(28) Sasongko, N. A.; Jeong, Y.; Paramita, S. A.; Heo, J.; Oh, M. H.; Reyes-Lillo, S. E.; Park, M. Role of Size and Shape in Photoluminescence and Ultra-Low-Frequency Raman of Methylammonium Lead Iodide Perovskite Quantum Dots. *J. Phys. Chem. Lett.* **2025**, *16*, 1522−1528.
(29) Chi, W.; Banerjee, S. K. Development of Perovskite Solar Cells by Incorporating Quantum Dots. *Chem. Eng. J.* **2021**, *426*, 131588.
(30) Xue, J.; Lee, J. W.; Dai, Z.; Wang, R.; Nuryyeva, S.; Liao, M. E.; Chang, S. Y.; Meng, L.; Meng, D.; Sun, P.; et al. Surface Ligand Management for Stable $FAPbI_3$ Perovskite Quantum Dot Solar Cells. *Joule* **2018**, *2* (9), 1866−1878.
(31) Wang, S.; Zhao, Q.; Hazarika, A.; Li, S.; Wu, Y.; Zhai, Y.; Chen, X.; Luther, J. M.; Li, G. Thermal Tolerance of Perovskite Quantum Dots Dependent on A-Site Cation and Surface Ligand. *Nat. Commun.* **2023**, *14* (1), 2216.
(32) Tan, M.; Chen, B.; Zhang, Y.; Ni, M.; Wang, W.; Zhang, H.; Zhou, Q.; Bao, Y.; Wang, Y. Temperature-Dependent Dynamic Carrier Process of $FAPbI_3$ Nanocrystals' Film. *J. Phys. Chem. C* **2020**, *124* (9), 5093−5098.
(33) Li, S.; Xia, J.; Wen, Z.; Gu, H.; Guo, J.; Liang, C.; Pan, H.; Wang, X.; Chen, S. The Formation Mechanism of (001) Facet Dominated α-$FAPbI_3$ Film by Pseudohalide Ions for High-Performance Perovskite Solar Cells. *Adv. Sci.* **2023**, *10* (18), 2300056.
(34) Ma, C.; Grätzel, M.; Park, N. G. Facet Engineering for Stable, Efficient Perovskite Solar Cells. *ACS Energy Lett.* **2022**, *7*, 3120−3128.
(35) Ma, C.; Kang, M. C.; Lee, S. H.; Kwon, S. J.; Cha, H. W.; Yang, C. W.; Park, N. G. Photovoltaically Top-Performing Perovskite Crystal Facets. *Joule* **2022**, *6* (11), 2626−2643.
(36) Mourdikoudis, S.; Menelaou, M.; Fiuza-Maneiro, N.; Zheng, G.; Wei, S.; Pérez-Juste, J.; Polavarapu, L.; Sofer, Z. Oleic Acid/Oleylamine Ligand Pair: A Versatile Combination in the Synthesis of Colloidal Nanoparticles. *Nanoscale Horiz.* **2022**, *7*, 941−1015.
(37) Akkerman, Q. A.; Motti, S. G.; Srimath Kandada, A. R.; Mosconi, E.; D'Innocenzo, V.; Bertoni, G.; Marras, S.; Kamino, B. A.; Miranda, L.; De Angelis, F.; et al. Solution Synthesis Approach to Colloidal Cesium Lead Halide Perovskite Nanoplatelets with Monolayer-Level Thickness Control. *J. Am. Chem. Soc.* **2016**, *138* (3), 1010−1016.
(38) De Trizio, L.; Infante, I.; Manna, L. Surface Chemistry of Lead Halide Perovskite Colloidal Nanocrystals. *Acc. Chem. Res.* **2023**, *56* (13), 1815−1825.
(39) Jeong, H. J.; Park, C.; Jeon, H.; Lee, K. N.; Lee, J.; Lim, S. C.; Namkoong, G.; Jeong, M. S. Quasi-2D Halide Perovskite Memory Device Formed by Acid-Base Binary Ligand Solution Composed of Oleylamine and Oleic Acid. *ACS Appl. Mater. Interfaces* **2021**, *13* (34), 40891−40900.
(40) Hao, M.; Bai, Y.; Zeiske, S.; Ren, L.; Liu, J.; Yuan, Y.; Zarrabi, N.; Cheng, N.; Ghasemi, M.; Chen, P.; et al. Ligand-Assisted Cation-Exchange Engineering for High-Efficiency Colloidal $Cs_{1-x}FA_xPbI_3$ Quantum Dot Solar Cells with Reduced Phase Segregation. *Nat. Energy* **2020**, *5* (1), 79−88.
(41) Almeida, G.; Goldoni, L.; Akkerman, Q.; Dang, Z.; Khan, A. H.; Marras, S.; Moreels, I.; Manna, L. Role of Acid-Base Equilibria in the Size, Shape, and Phase Control of Cesium Lead Bromide Nanocrystals. *ACS Nano* **2018**, *12* (2), 1704−1711.
(42) Kosugi, T.; Iso, Y.; Isobe, T. Effects of Oleic Acid on the Stability of Perovskite $CsPbBr_3$ Quantum Dot Dispersions. *Chem. Lett.* **2019**, *48* (4), 349−352.
(43) Chen, D.; Chen, X. Luminescent Perovskite Quantum Dots: Synthesis, Microstructures, Optical Properties and Applications. *J. Mater. Chem. C* **2019**, *7*, 1413−1446.
(44) Zhang, J.; Zhang, S.; Zhang, Y.; Al-Hartomy, O. A.; Wageh, S.; Al-Sehemi, A. G.; Hao, Y.; Gao, L.; Wang, H.; Zhang, H. Colloidal Quantum Dots: Synthesis, Composition, Structure, and Emerging Optoelectronic Applications. *Laser. Photonics. Rev.* **2023**, *17* (3), 2200551.
(45) Wright, A. D.; Verdi, C.; Milot, R. L.; Eperon, G. E.; Pérez-Osorio, M. A.; Snaith, H. J.; Giustino, F.; Johnston, M. B.; Herz, L. M. Electron-Phonon Coupling in Hybrid Lead Halide Perovskites. *Nat. Commun.* **2016**, *7*, 11755.
(46) Strandell, D. P.; Kambhampati, P. The Temperature Dependence of the Photoluminescence of $CsPbBr_3$ Nanocrystals Reveals Phase Transitions and Homogeneous Linewidths. *J. Phys. Chem. C* **2021**, *125* (49), 27504−27508.
(47) Wang, X.; Wang, Q.; Chai, Z.; Wu, W. The Thermal Stability of $FAPbBr_3$ nanocrystals from Temperature-Dependent Photoluminescence and First-Principles Calculations. *RSC Adv.* **2020**, *10* (72), 44373−44381.
(48) Greenland, C.; Shnier, A.; Rajendran, S. K.; Smith, J. A.; Game, O. S.; Wamwangi, D.; Turnbull, G. A.; Samuel, I. D. W.; Billing, D. G.; Lidzey, D. G. Correlating Phase Behavior with Photophysical Properties in Mixed-Cation Mixed-Halide Perovskite Thin Films. *Adv. Energy Mater.* **2020**, *10* (4), 1901350.
(49) Fu, M.; Tamarat, P.; Trebbia, J. B.; Bodnarchuk, M. I.; Kovalenko, M. V.; Even, J.; Lounis, B. Unraveling Exciton−Phonon Coupling in Individual $FAPbI_3$ Nanocrystals Emitting near-Infrared Single Photons. *Nat. Commun.* **2018**, *9* (1), 3318.
(50) Woo, H. C.; Choi, J. W.; Shin, J.; Chin, S. H.; Ann, M. H.; Lee, C. L. Temperature-Dependent Photoluminescence of $CH_3NH_3PbBr_3$ Perovskite Quantum Dots and Bulk Counterparts. *J. Phys. Chem. Lett.* **2018**, *9* (14), 4066−4074.
(51) Peng, H.; Zou, B. Effects of Electron-Phonon Coupling and Spin-Spin Coupling on the Photoluminescence of Low-Dimensional Metal Halides. *J. Phys. Chem. Lett.* **2022**, *13*, 1752−1764.
(52) Luo, J.; Wang, X.; Li, S.; Liu, J.; Guo, Y.; Niu, G.; Yao, L.; Fu, Y.; Gao, L.; Dong, Q.; et al. Efficient and Stable Emission of Warm-White Light from Lead-Free Halide Double Perovskites. *Nature* **2018**, *563* (7732), 541−545.
(53) Chen, T.; Chen, W. L.; Foley, B. J.; Lee, J.; Ruff, J. P. C.; Ko, J. Y. P.; Brown, C. M.; Harriger, L. W.; Zhang, D.; Park, C.; et al. Origin of Long Lifetime of Band-Edge Charge Carriers in Organic−Inorganic Lead Iodide Perovskites. *Proc. Natl. Acad. Sci. U.S.A.* **2017**, *114* (29), 7519−7524.
(54) Weber, O. J.; Ghosh, D.; Gaines, S.; Henry, P. F.; Walker, A. B.; Islam, M. S.; Weller, M. T. Phase Behavior and Polymorphism of Formamidinium Lead Iodide. *Chem. Mater.* **2018**, *30* (11), 3768−3778.
(55) Sun, S.; Deng, Z.; Wu, Y.; Wei, F.; Halis Isikgor, F.; Brivio, F.; Gaultois, M. W.; Ouyang, J.; Bristowe, P. D.; Cheetham, A. K.; et al. Variable Temperature and High-Pressure Crystal Chemistry of Perovskite Formamidinium Lead Iodide: A Single Crystal X-Ray Diffraction and Computational Study. *Chem. Commun.* **2017**, *53* (54), 7537−7540.
(56) Kawachi, S.; Atsumi, M.; Saito, N.; Ohashi, N.; Murakami, Y.; Yamaura, J. I. Structural and Thermal Properties in Formamidinium and Cs-Mixed Lead Halides. *J. Phys. Chem. Lett.* **2019**, *10* (22), 6967−6972.
(57) Lavén, R.; Koza, M. M.; Malavasi, L.; Perrichon, A.; Appel, M.; Karlsson, M. Rotational Dynamics of Organic Cations in Formamidinium Lead Iodide Perovskites. *J. Phys. Chem. Lett.* **2023**, *14* (11), 2784−2791.
(58) Kovalenko, M. V.; Protesescu, L.; Bodnarchuk, M. I. Properties and Potential Optoelectronic Applications of Lead Halide Perovskite Nanocrystals. *Science* **2017**, *358* (6364), 745−750.

https://doi.org/10.1021/acs.jpcc.5c05144
J. Phys. Chem. C 2025, 129, 15342−15350

(59) Driscoll, E. H.; Orera, A.; Anderson, P. A.; Sanjuán, M. L.; Slater, P. R. Raman Spectroscopy Insights into the α- And δ-Phases of Formamidinium Lead Iodide ($FAPbI_3$). *Dalton Trans.* **2021**, *50* (9), 3315−3323.
(60) Galatopoulos, F.; Papagiorgis, P.; Ioakeimidis, A.; Chrusou, A. Z.; Souzou, A.; Christodoulou, C.; Bernasconi, C.; Bodnarchuk, M. I.; Leontidis, E.; Kovalenko, M. V.; et al. Photovoltaic Limitations of $FAPbI_3$ Nanocrystal Solar Cells Associated with Ligand Washing Processes. *APL Energy* **2024**, *2* (1), 016101.
(61) Diroll, B. T.; Guo, P.; Schaller, R. D. Unique Optical Properties of Methylammonium Lead Iodide Nanocrystals below the Bulk Tetragonal-Orthorhombic Phase Transition. *Nano Lett.* **2018**, *18* (2), 846−852.
(62) Mishra, A.; Hope, M. A.; Grätzel, M.; Emsley, L. A Complete Picture of Cation Dynamics in Hybrid Perovskite Materials from Solid-State NMR Spectroscopy. *J. Am. Chem. Soc.* **2023**, *145* (2), 978−990.
(63) He, Y.; Yan, J.; Xu, L.; Zhang, B.; Cheng, Q.; Cao, Y.; Zhang, J.; Tao, C.; Wei, Y.; Wen, K.; et al. Perovskite Light-Emitting Diodes with Near Unit Internal Quantum Efficiency at Low Temperatures. *Adv. Mater.* **2021**, *33* (14), 2006302.
(64) Wei, Q.; Liang, H.; Haruta, Y.; Saidaminov, M.; Mi, Q.; Saliba, M.; Cui, G.; Ning, Z. From Tetragonal to Cubic: Perovskite Phase Structure Evolution for High-Performance Solar Cells. *Sci. Bull.* **2023**, *68*, 141−145.
(65) Zhou, B.; Zhao, P.; Guo, J.; Hu, S.; Guo, X.; Liu, J.; Li, C. Unveiling the Importance of Nondominant Facets in (111)-Dominated Perovskite Films. *ACS Appl. Mater. Interfaces* **2025**, *17* (15), 22715−22726.
(66) Yang, T.; Yang, Y.; Niu, T.; Zhao, E.; Wu, N.; Wang, S.; Chen, X.; Wang, S.; Wang, Y.; Wu, Y.; et al. Facet Orientation-Dependent Strain Relaxation Stabilizes $FAPbI_3$ Perovskite Solar Cells. ACS Energy. *Lett.* **2025**, *10* (1), 427−438.
(67) Woo, H.; Choi, J.; Shin, J.; Chin, S.; Ann, M.; Lee, C. Temperature-Dependent Photoluminescence of $CH_3NH_3PbBr_3$ Perovskite Quantum Dots and Bulk Counterparts. *J. Phys. Chem. Lett.* **2018**, *9* (14), 4066−4074.
(68) Bornschlegl, A.; Lichtenegger, M.; Luber, L.; Lampe, C.; Bodnarchuk, M.; Kovalenko, M.; Urban, A. Dark-Bright Exciton Splitting Dominates Low-Temperature Diffusion in Halide Perovskite Nanocrystal Assemblies. *Adv. Energy Mater.* **2024**, *14*, 2303312.
(69) Tress, W.; Domanski, K.; Carlsen, B.; Agarwalla, A.; Alharbi, E. A.; Graetzel, M.; Hagfeldt, A. Performance of Perovskite Solar Cells under Simulated Temperature-Illumination Real-World Operating Conditions. *Nat. Energy* **2019**, *4* (7), 568−574.
(70) Deng, W.; Wei, J.; Ma, Z.; Feng, W. Research Progress on Stability of $FAPbI_3$ Perovskite Solar Cells. *Cryst. Res. Technol.* **2025**, *60* (2), 2400228.
(71) Tu, Y.; Wu, J.; Xu, G.; Yang, X.; Cai, R.; Gong, Q.; Zhu, R.; Huang, W. Perovskite Solar Cells for Space Applications: Progress and Challenges. *Adv. Mater.* **2021**, *33* (21), 2006545.
(72) Wang, M.; Yang, Z.; Chen, Y.; Shi, L.; Cao, K.; Liang, Y.; Cao, G.; Li, X.; Qin, L. Understanding Temperature-Induced Performance Degradation in Perovskite/Silicon Tandem Solar Cells. *Sol. Energy Mater. Sol. Cells* **2025**, *282*, 113393.
(73) Kolobkova, E. V.; Semaan, R.; Kuznetsova, M. S.; Nikonorov, N. V. High-Temperature Photoluminescence of $CsPbBr_3$ Perovskite Nanocrystals in the Fluorophosphate Glasses. *J. Lumin.* **2023**, *255*, 119541.
(74) Heo, J.; Kim, H.; Park, J.; Sasongko, N. A.; Jeong, M.; Han, J.; Seo, T.; Ji, Y.; Han, J.; Park, M. Long-Term Comparisons of Photoluminescence Affected by Organic Cations of Formamidinium and Methylammonium in Monophasic Lead Iodide Perovskite Quantum Dots. *Chem. Asian. J.* **2024**, *19*, No. e202400347.

https://doi.org/10.1021/acs.jpcc.5c05144
J. Phys. Chem. C 2025, 129, 15342−15350